



## Article

# CO<sub>2</sub> Leakage Scenarios in Shale Overburden

Gilda Currenti <sup>1,\*</sup>, Barbara Cantucci <sup>1</sup>, Giordano Montegrossi <sup>2,3</sup>, Rosalba Napoli <sup>1</sup>, M. Shahir Misnan <sup>4</sup>, M. Rashad Amir Rashidi <sup>4</sup>, Zainol Affendi Abu Bakar <sup>4</sup>, Zuhar Zahir Tuan Harith <sup>5</sup>, Nabila Hannah Samsol Bahri <sup>5</sup> and Noorbaizura Hashim <sup>5</sup>

<sup>1</sup> Istituto Nazionale di Geofisica e Vulcanologia, Via di Vigna Murata 605, 00143 Rome, Italy; barbara.cantucci@ingv.it (B.C.); rosalba.napoli@ingv.it (R.N.)

<sup>2</sup> Centro Nazionale delle Ricerche-Istituto di Geoscienze e Georisorse, Via G. La Pira 4, 50121 Firenze, Italy; giordano.montegrossi@igg.cnr.it

<sup>3</sup> Consorzio Interuniversitario Nazionale per la Scienza e Tecnologia dei Materiali-INSTM, Via G. Giusti 9, 50121 Firenze, Italy

<sup>4</sup> PETRONAS Research Sdn. Bhd, Bandar Baru Bangi 43650, Malaysia; shahir.misnan@petronas.com (M.S.M.); mrashad.amirrashidi@petronas.com (M.R.A.R.); zainolaffendi\_abubakar@petronas.com (Z.A.A.B.)

<sup>5</sup> AEM Energy Solutions Sdn. Bhd, Kuala Lumpur 50450, Malaysia; zahir.harith@gmail.com (Z.Z.T.H.); nabila.sbj@aemenersol.com (N.H.S.B.); noorbaizura.hashim@aemenersol.com (N.H.)

\* Correspondence: gilda.currenti@ingv.it

**Abstract:** Potential CO<sub>2</sub> leakage from deep geologic reservoirs requires evaluation on a site-specific basis to assess risk and arrange mitigation strategies. In this study, a heterogeneous and realistic numerical model was developed to investigate CO<sub>2</sub> migration pathways and uprising time in a shaly overburden, located in the Malaysian off-shore. Fluid flow and reactive transport simulations were performed by TOUGHREACT to evaluate the: (1) seepage through the caprock; (2) CO<sub>2</sub>-rich brine leakage through a fault connecting the reservoir with seabed. The effect of several factors, which may contribute to CO<sub>2</sub> migration, including different rock types and permeability, Fickian and Knudsen diffusion and CO<sub>2</sub> adsorption in the shales were investigated. Obtained results show that permeability mainly ruled CO<sub>2</sub> uprising velocity and pathways. CO<sub>2</sub> migrates upward by buoyancy without any important lateral leakages due to poor-connection of permeable layers and comparable values of vertical and horizontal permeability. Diffusive flux and the Knudsen flow are negligible with respect to the Darcy regime, despite the presence of shales. Main geochemical reactions deal with carbonate and pyrite weathering which easily reach saturation due to low permeability and allowing for re-precipitation as secondary phases. CO<sub>2</sub> adsorption on shales together with dissolved CO<sub>2</sub> constituted the main trapping mechanisms, although the former represents likely an overestimation due to estimated thermodynamic parameters. Developed models for both scenarios are validated by the good agreement with the pressure profiles recorded in the exploration wells and the seismic data along a fault (the F05 fault), suggesting that they can accurately reproduce the main processes occurring in the system.

**Keywords:** carbon capture and storage; CO<sub>2</sub> migration; fluid flow and reactive transport simulations; Sarawak Basin



**Citation:** Currenti, G.; Cantucci, B.; Montegrossi, G.; Napoli, R.; Misnan, M.S.; Rashidi, M.R.A.; Abu Bakar, Z.A.; Harith, Z.Z.T.; Bahri, N.H.S.; Hashim, N. CO<sub>2</sub> Leakage Scenarios in Shale Overburden. *Minerals* **2023**, *13*, 1016. <https://doi.org/10.3390/min13081016>

Academic Editor: Rafael Santos

Received: 26 May 2023

Revised: 25 July 2023

Accepted: 27 July 2023

Published: 29 July 2023



**Copyright:** © 2023 by the authors. Licensee MDPI, Basel, Switzerland. This article is an open access article distributed under the terms and conditions of the Creative Commons Attribution (CC BY) license (<https://creativecommons.org/licenses/by/4.0/>).

## 1. Introduction

Carbon capture and storage (CCS) is a promising technology able to stabilize and reduce the atmospheric concentration of anthropogenic CO<sub>2</sub> by storing this greenhouse gas underground in deep geologic formations [1–3]. In order to minimize hazards associated with this technology and to ensure a safe storage of CO<sub>2</sub> at depth, possible leakage risks from the reservoir have to be carefully evaluated.

Three main leakage processes in CO<sub>2</sub> storage are commonly reported in literature [4–7]: (1) over-pressurization in the CO<sub>2</sub> storage reservoir that exceeds the capillary breakthrough pressure of the caprock [8], (2) leakage through fault/fracture systems that forms due

to regional tectonic, fault reactivation or creation of new fractures if injection exceed the minimum rock strength [9,10], and (3) chemical degradation and/or mechanical failure of the cementing of uncased, poorly maintained or undocumented wells [11,12].

Although porosity, permeability, capillary entry pressure [13–15] and injection pressure [7] mainly control the fluid flow and the transport processes in porous media, CO<sub>2</sub> migration can be also ruled by chemical processes. CO<sub>2</sub>, indeed, is a highly reactive fluid and when it comes into contact with the host rock and the caprock can produce minerals alteration which may, in turn, sensibly alter porosity and permeability [16]. Therefore, the effect of geochemistry on fluid flow should be always considered [17].

In the frame of a feasibility study for CO<sub>2</sub> storage—Enhanced Gas Recovery (EGR), the goal of this paper is to evaluate the overburden capacity to retain CO<sub>2</sub> at depth and investigate possible migration pathways and the uprising timescale of CO<sub>2</sub> in case of leakage. The structure we focused on is located in a basin off-shore Malaysia and consists of a carbonate gas field with a heavy CO<sub>2</sub> contamination of 70%, overlined by a heterogeneous shaly overburden. Fluid-flow and reactive transport models were simulated by TOUGHREACT code [18,19] to achieve our objective. In particular, we investigated the CO<sub>2</sub> leakage from the top of the reservoir into the overburden (Scenario 1) and the leakage of CO<sub>2</sub> throughout a fault connecting the reservoir with the seabed (Scenario 2; Figure 1). We neglected leakage from wells since it is strictly dependent on well-bore built characteristics (e.g., cement type, casing).

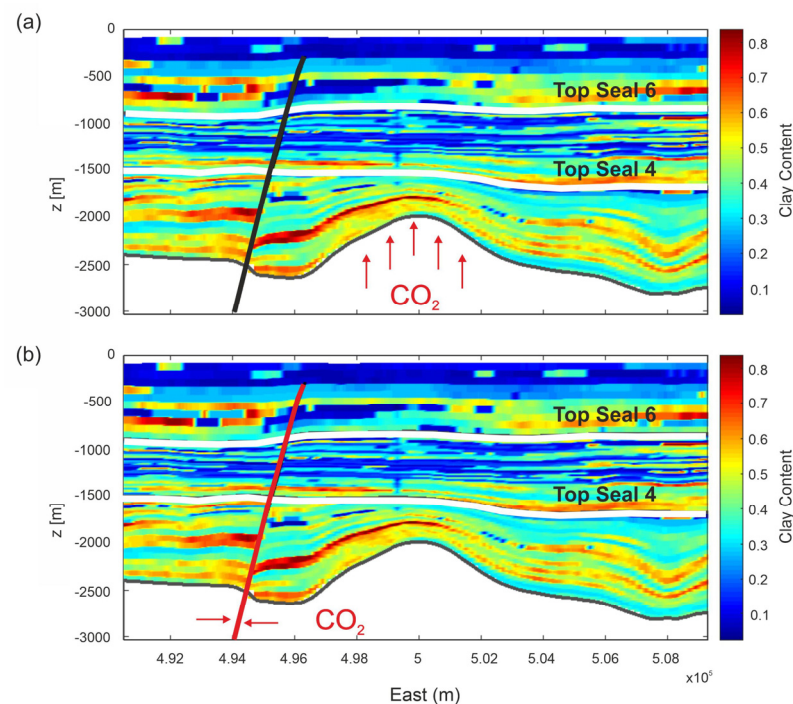


**Figure 1.** 2D sections of selected structures showing the investigated CO<sub>2</sub> leakage scenarios: (a) overpressurization of carbonate reservoir; (b) leakage through the FO5 fault. The legend represents the clay content of rock formations (volume fraction). White lines highlight the Seal 6 and Seal 4 horizons. The black (not active) and red (active) lines represent the FO5 fault.

Numerical simulations of shale overburden are challenging since the porous medium is not homogeneous, and the permeability is generally low. Therefore, a realistic representation of heterogeneity is a pre-requisite to effectively predict the CO<sub>2</sub> migration pathways [20,21] along the overburden. In shales, which contain very narrow pores with a diameter comparable to the mean free path of the gas molecules, non-Darcy flow conditions may be established [22]. In such a case, gaseous molecules will collide more often with the pore walls and not very frequently with other molecules [23,24]. This additional flux, due to molecular interaction with porous medium [23], enhances the gas flow rate and should be considered in the models together with advective flow.

Shale contain clay minerals and organic matter. Due to its micropore structure, shale has the capacity to absorb CO<sub>2</sub>, mitigating leakage impact in case of CO<sub>2</sub> migrating throughout the caprock. Indeed, the very narrow pores of shales create intimate fluid-rock interactions that could lead to the physical adsorption of gas, trapping leaked CO<sub>2</sub> [7]. Ref. [25] investigated the CO<sub>2</sub> sorption capacity for Belgium black shale which is about 7.9 kg/t of the formation, while [26] showed the sorption capacity for CO<sub>2</sub> is around 5.5 kg/t for the Muderong Shale (Australia).

Depending on specific objectives, numerical modelling studies often considered the above mentioned topics separately and/or used a simplified approach to optimize the computational effort. As an example, the heterogeneity of the porous medium was often not taken into account or was analyzed using geostatistical approaches and random models [27] resulting in less accurate prediction of the subsurface plume behavior [28]. As an alternative, coarse grids were employed by upscaling rock properties to reduce the cells number thus incurring in an overestimation of CO<sub>2</sub> solubility [29] and migration velocity [28]. On the contrary, simulations involving high resolution models considered a limited extension of the domain [20].

In numerical simulations, geochemical processes are sometimes neglected because the time-scale for reactions is retained too long to have significant effect in the short time, thus missing the effect of fast-kinetic minerals on fluid flow. Moreover, performing fully coupled reactive transport models is still challenging due to the low computational efficiency of multiphase flow, especially when pertinent mineralogical assemblage is considered [30,31].

Finally, gas adsorption, non-Darcy flow and Fickian diffusion are significant mechanisms but they are generally considered only in shale-gas reservoir modelling [32] without coupling geochemical reactions.

With respect to previous works, this study attempts to investigate at the same time various key processes of fluid migration in heterogeneous shaly overburden as Knudsen diffusion, Fickian molecular diffusion, CO<sub>2</sub> sorption on clays and the effects of geochemical reactions on CO<sub>2</sub> migration. A very realistic numerical model was developed by using the large amount of available site-specific data, obtained during the well drilling as cores, wireline logs, seismic data, laboratory analyses and experiments. This site-specific information provided an accurate description of 3D strata geometry and lithology, porosity and permeability distributions in the reservoir and in the overburden formations.

Understanding the effects of these phenomena on fluid flow will help us effectively improve our knowledge on fluid migration throughout shales. Moreover, due to the widespread diffusion of shaly overburden, the results obtained in this study can be easily exported to other sites potentially suitable for CO<sub>2</sub> geological storage.

## 2. Site Description and Characterization

The investigated area is located north of Central Luconia Province offshore Sarawak Basin, East Malaysia. The Luconia Province, extends for 240 × 240 km and is one of the largest of the southeast Asia carbonate provinces [33]. Its structural-stratigraphy evolution is closely related to the opening of the South China Sea [34–36] which started in the Oligocene and has established a regional pattern of horst and graben structures [37]. During Early to Late Miocene carbonate deposition started on structural highs of siliciclastics [38] and over 250 carbonate platforms have formed across the province. The interplay among eustatic sea-level, basinal tectonics and clastic sediment supply, governed intermittent carbonate and siliciclastic deposition, producing VIII regional cycles with several transgressive and regressive sequences. The structure, on which this study focuses, is constituted by Pliocene sediments (VI and VII cycles), separated by rapid and widespread transgressions discordantly overlaying a middle Miocene carbonate reservoir (V cycle). The overburden formations consist mainly of interbedded silt, silty clay and shale intervals and can be divided in three main horizons based on the contrast in sonic-log velocity (from the top): soft sediments lying below sea bed, the Seal 6 and the Seal 4 overlying the reservoir (Figure 1). Based on the quick correlation of lithofacies from well log information, the presence of silt layers is prominent in Seal 6, while the shale dominates Seal 4 with some intercalation of

silt. The carbonate reservoir, hosting a saline aquifer (26 g/L), is approximately 2 km below sea-level, where the water depth is about 120 m. A gas cap contaminated by 70% of CO<sub>2</sub> is present, with a water-gas contact at 2200 m depth.

Several faults, connecting the reservoir to the overburden, are present in the investigated system. All of them remain within the Seal 4 top except the FO5, which connects the reservoir to soft sediments reaching 300 m depth.

Three wells were drilled to investigate the structure, providing the main information about lithology, geothermal and geobaric gradients. Petrophysical investigations (i.e., X-Ray Diffraction combined with Rietveld refinement, X-Ray Fluorescence, electron microscopy and microanalysis), carried out on core samples [39], show that the shaly overburden (Seal 6 and Seal 4 formations) is mainly composed of quartz and anorthite (from 35 to 51% *w/w*). Fe-Illite, kaolinite and chlorite participate from 31 to 40% *w/w* with minor Fe-muscovite (11% *w/w*). Finally, minor amounts of calcite, dolomite and Fe-rich carbonates belonging to dolomite-ankerite series are present (from 7 to 14% *w/w*). Unfortunately, core samples of soft sediments were not available for analysis. The carbonate reservoir is mainly constituted by calcite, dolomite and Fe-rich carbonates belonging to dolomite-ankerite series (76% *w/w*). Minor quartz, anorthite, Fe-muscovite (14% *w/w*) and clay minerals (Fe-illite, chlorite and kaolinite, 10% *w/w*) are also present. Pyrite is present in all the samples even if in unquantifiable amounts (<1% *w/w*).

Temperature and pressure gradients show a hydrostatic trend from the surface to around 1400 m depth (76 °C and 15 MPa), roughly corresponding to Seal 4 top. From this horizon to the reservoir a high temperature-high pressure zone is present (about 133 °C and 315 MPa at about 1900 m, top reservoir).

### 3. Numerical Modeling

TOUGHREACT V2 [18,19] code is used to perform a fully-coupled, simultaneous solution of mass and energy balance for multi-component, multi-phase fluids in permeable media coupled with a multiphase extension of Darcy's Law. The full description of the TOUGHREACT governing equations are reported in [19].

The hot fluid circulation in the system is simulated using a modified ECO<sub>2</sub>N module (see Section 3.1), which incorporates CO<sub>2</sub>-H<sub>2</sub>O equations of state in the temperature and pressure range 0–300 °C and 0–600 bar, respectively. The contribution of the other gasses present in the gas cap was neglected.

The relative permeability of gas and liquid phases is calculated from the van Genuchten-Mualem model [40,41] and capillary pressures from van Genuchten's function [41] according to the method described by [42]. The parameters used for these functions (Table 1) were indirectly obtained by MICP analysis [39] on core samples for Seal 6, Seal 4 and reservoir, after conversion from mercury to subsurface CO<sub>2</sub>-water values.

**Table 1.** Parameter for TOUGHREACT capillary pressure [41] and relative permeability [40,41] functions.

Sample	$\lambda$	$S_{lr}$	$1/P_0$	P	$S_{gr}$
Seal 6—soft sediments	0.243	0.274	$3.211 \times 10^{-8}$	$1.200 \times 10^8$	0.041
Seal 4	0.223	0.209	$2.872 \times 10^{-7}$	$1.200 \times 10^8$	0.051
Reservoir	0.327	0.539	$8.412 \times 10^{-8}$	$1.200 \times 10^8$	0.008

$\lambda$ : is the van Genuchten pore-size distribution index, obtained by fitting MICP data;  $S_{lr}$ : irreducible liquid saturation;  $P_0$ : pressure scaling parameter; P: maximum capillary pressure;  $S_{gr}$ : irreducible gas saturation.

Molecular diffusion was considered in simulating transport of aqueous CO<sub>2</sub>. As shown by [39,43] geochemical reactions and adsorption on shales can significantly retard CO<sub>2</sub> diffusion front where the concentration gradient is larger. Therefore, two different diffusion coefficients were used for fluid flow and reactive transport simulations. A constant value of  $2.8 \times 10^{-11}$  m<sup>2</sup>/s, obtained by reaction-diffusion laboratory experiments, performed on core samples [39] at in-situ condition, was used for the fluid flow model; whereas a coefficient of  $1.61 \times 10^{-10}$  m<sup>2</sup>/s was applied for the reactive transport model. The lat-



ter was computed reproducing, by modeling with TOUGHREACT, the reaction-diffusion laboratory experiments and considering CO<sub>2</sub> adsorption and geochemical reactions (see Section 3.3) processes. No temperature and pressure dependence of diffusion coefficient was modelled, since CO<sub>2</sub> reaction-diffusion experiments show comparable values ranging from 2.8 to 3.12 × 10<sup>-11</sup> m<sup>2</sup>/s after 5 days at different temperatures (75, 105 and 145 °C) [39].

In order to take into account also the non-Darcy flow regime, Knudsen diffusion [44] was included in the model. In TOUGHREACT the Knudsen diffusion is simulated by correcting the permeability as a function of the pressure:

$$k_a = k \left( 1 + \frac{b}{P} \right) \quad (1)$$

where  $k_a$  is gas permeability (m<sup>2</sup>);  $k$  is permeability at infinite pressure (m<sup>2</sup>),  $P$  is pressure (MPa) and  $b$  is the Klinkenberg slippage factor (MPa) [44] which is used to calibrate permeability measurements when the pore space approaches the mean free path of the gas. Based on N<sub>2</sub> permeameter measurements on the core samples, a  $b$  value of about 0.07 MPa was estimated and employed in the model.

### 3.1. Code Modification

The original TOUGHREACT V2 code by means of the ECO<sub>2</sub>N model [45,46] reproduces fluid properties for temperature and pressure within the ranges 10 °C < T < 110 °C,  $p < 600$  bar, and salinity conditions up to halite saturation. To simulate the relatively high temperature gradient of the investigated site, TOUGHREACT source code was modified to account for temperatures up to about 300 °C and for the effect of water on thermo-physical properties of CO<sub>2</sub> rich phase (according to [46]), excluding water boiling. This includes density, viscosity, and specific enthalpy of fluid phases as functions of temperature, pressure and composition, as well as partitioning of mass components H<sub>2</sub>O, NaCl and CO<sub>2</sub> among the different phases.

The modified code uses the original model for mass partitioning of [46] but includes also the new high temperature model (>109 °C) of [47]. The modified code was validated by comparisons with the results reported in [47] and in the TOUGH2-ECO<sub>2</sub>H manual [48].

### 3.2. Geochemical Modeling

Geochemical calculations were performed under the local equilibrium assumption for aqueous species, whereas mineral dissolution and precipitation proceeded under kinetic conditions. The general transition state theory [49–51] equation (Equation (2)), which includes temperature dependence of the rate constants and reaction terms for acid (H<sup>+</sup>) and neutral mechanisms [50,52,53], was used. For carbonate reactions, the carbonate mechanism [54], which includes the reaction order  $n$  with respect to PCO<sub>2</sub>, was also considered.

$$r = S \left[ \left( k_{298-acid} \exp \left[ \frac{-E_a-acid}{R} \left( \frac{1}{T} - \frac{1}{298.15} \right) \right] a_{H^+}^{n1} \right) + \left( k_{298-neut} \exp \left[ \frac{-E_a-neut}{R} \left( \frac{1}{T} - \frac{1}{298.15} \right) \right] \right) + \left( k_{298-base} \exp \left[ \frac{-E_a-base}{R} \left( \frac{1}{T} - \frac{1}{298.15} \right) \right] a_{OH^-}^{n1} \right) \right] (1 - \Omega) \quad (2)$$

where  $r$  is the kinetic rate (mol/m<sup>2</sup> s; positive values indicate dissolution, while negative values refer precipitation),  $S$  is the specific reactive surface area (m<sup>2</sup>/g),  $k_{298.15}$  is the rate constant at 298.15 K (mol/m<sup>2</sup> s),  $E_a$  is the activation energy (J/mol),  $R$  is the gas constant (8.314 J/molK),  $T$  is the absolute temperature (K),  $a$  is the aqueous activity of the species,  $n$  is the order of the reaction, and  $\Omega$  is the mineral saturation index.

All the kinetic parameters employed in Equation (2) are taken from [52]. In the model we used the siderite as a proxy for Fe-rich carbonates belonging to dolomite-ankerite series, to take into account the non-negligible iron content (3.69%–17.78%) observed at SEM-EDS analyses [39]. Reaction-diffusion experiments performed on core samples show comparable alteration velocity of calcite and Fe-rich carbonates at the CO<sub>2</sub> reaction front, after 2 and

5 days [39]. Therefore, we used the same kinetic parameters for calcite and siderite. Values of muscovite and smectite were used as proxy for Fe-muscovite and Fe-illite, respectively.

Specific reactive area of minerals (Table 2) was computed as geometric area on the basis of SEM-EDS images [39] assuming that mineral grains have spherical, cylindrical or plate-like shape. The geometric area was calibrated by a numerical model with TOUGHREACT reproducing diffusion experiments (see Section 3.3).

**Table 2.** Mineralogical composition (volume fraction) and specific reactive area ( $S, \text{m}^2/\text{m}^3$ ) used in reactive transport model (RTM) simulations. Laboratory data (XRD, XRF, SEM-EDS) of Seal 4 and Seal 6 were recomputed in function of the 7 clay content classes identified. For reservoir formation no clay content classes were defined due to the low content.

Clay Class	0–0.063	0.063–0.142	0.142–0.282	0.282–0.422	0.422–0.562	0.562–0.702	>0.702	Res.	$S \cdot 10^6 (\text{m}^2/\text{m}^3)$
Seal 4									
Kaolinite	1.16	3.76	7.78	12.92	18.06	23.20	28.27		6.38
Fe-Illite	1.91	6.20	12.83	21.30	29.77	38.24	46.59		4.50
Chlorite	0.09	0.29	0.59	0.98	1.37	1.76	2.15		5.11
Quartz	52.90	48.95	42.85	35.06	27.27	19.48	11.79		1.78
Fe-celadonite (Fe-muscovite)	17.46	16.18	14.21	11.68	9.16	6.63	4.14		3.58
Anorthite	7.23	6.70	5.88	4.84	3.79	2.75	1.72		2.34
Siderite	11.38	10.54	9.26	7.61	5.97	4.32	2.70		2.15
Dolomite	5.08	4.71	4.14	3.40	2.67	1.93	1.21		1.19
Calcite	1.80	1.67	1.47	1.21	0.95	0.69	0.43		1.32
Pyrite	-	-	-	-	-	-	-		0.09
Seal 6									
Kaolinite	0.83	2.69	5.56	9.23	12.90	16.57	20.19		17.73
Fe-Illite	2.01	6.53	13.50	22.41	31.33	40.24	49.03		12.50
Chlorite	0.32	1.04	2.14	3.56	4.97	6.39	7.78		14.20
Quartz	55.07	50.96	44.62	36.51	28.41	20.30	12.31		4.83
Fe-celadonite (Fe-muscovite)	13.77	12.76	11.20	9.21	7.22	5.23	3.27		9.95
Anorthite	17.03	15.78	13.86	11.39	8.93	6.47	4.04		6.50
Siderite	3.93	3.64	3.20	2.63	2.06	1.49	0.93		5.98
Dolomite	3.43	3.18	2.79	2.30	1.80	1.30	0.81		3.30
Calcite	2.62	2.43	2.13	1.75	1.37	1.00	0.62		1.32
Pyrite	-	-	-	-	-	-	-		0.02
Reservoir									
Kaolinite								4.70	17.73
Fe-Illite								3.85	12.50
Chlorite								1.59	14.20
Quartz								10.04	4.83
Fe-celadonite (Fe-muscovite)								1.57	9.95
Anorthite								2.05	6.50
Siderite								0.64	5.98
Dolomite								11.63	3.30
Calcite								63.94	0.99
Pyrite								1.00	0.05

Thermodynam database [55] was re-computed by SUPCRT92 [56] code at a pressure of 22.6 MPa, representing the centroid pressure of the structure.

$\text{CO}_2$  adsorption in clay rocks was modelled by adding a fake “mineral” ( $\text{CO}_{2\text{ads}}$ ) to the thermodynamic database. This approach allowed us to simulate chemical reactions between the surface of the adsorbent (clays) and the adsorbate molecules ( $\text{CO}_2$ ) as a function of clay minerals volume fraction and  $\text{PCO}_2$ . [57] evaluated the  $\text{CO}_2$  sorption potential on shales and provided fitting parameters of experimental data for Langmuir, Freundlich and Toth isotherm equations at 473, 623 and 773 K. In this work, Freundlich model (Equation (3)) with  $k_F$  and  $m$  parameters [57] was chosen because the  $\text{CO}_2$  partial pressure (term  $P$ ) is internally computed in TOUGHREACT:

$$C = k_F \times P^{1/m} \quad (3)$$

where  $C$  (mmol/g) is the amount of  $\text{CO}_2$  adsorbed,  $k_F$  is the Freundlich equilibrium constant (mmol  $\text{kPa}^m/\text{g}$ ),  $m$  is a parameter reflecting the heterogeneity of the system [58] and  $P$  is the  $\text{CO}_2$  partial pressure.

To rewrite the Freundlich adsorption isotherm in the TOUGHREACT database formalism, i.e., using  $\text{HCO}_3^-$  and  $\text{H}^+$  as primary species, we can consider the following equation:

$$P_{\text{CO}_2} = \frac{[\text{H}^+][\text{HCO}_3^-]}{k_1 k_h} \quad (4)$$

and substitute the  $P_{\text{CO}_2}$  (Equation (4)) in Equation (3), thus obtaining:

$$\log [C_{\text{ads}}] = \log k_F + \frac{1}{m} (\log [\text{H}^+] + \log [\text{HCO}_3^-] - \log k_1 - \log k_h) \quad (5)$$

where  $C_{\text{ads}}$  is the amount of adsorbed  $\text{CO}_2$  in shales,  $[\text{H}^+]$  and  $[\text{HCO}_3^-]$  are the activities of ionic species,  $k_1$  and  $k_h$  are the equilibrium constant of carbonic acid dissociation and the solubility constant of  $\text{CO}_2$ , respectively.

$\text{Log}C_{\text{ads}}$  were computed using  $k_F$  and  $m$  parameters as provided at temperatures of 473, 623 and 773 K [57] and further interpolated to temperatures required by TOUGHREACT database (Table 3). To compute  $\text{CO}_{2\text{ads}}$  equilibrium constants, the dissolution reaction reported in Table 3 was added in the thermodynamic database.

**Table 3.** Dissolution reaction and relative equilibrium constant ( $\text{Log}C_{\text{ads}}$ ) of  $\text{CO}_{2(\text{ads})}$  phase added to the THERMOTDEM database.

Mineral	Dissolution Reaction	$\text{Log}C_{\text{ads}}$ 0 °C	$\text{Log}C_{\text{ads}}$ 25 °C	$\text{Log}C_{\text{ads}}$ 60 °C	$\text{Log}C_{\text{ads}}$ 100 °C	$\text{Log}C_{\text{ads}}$ 150 °C	$\text{Log}C_{\text{ads}}$ 200 °C	$\text{Log}C_{\text{ads}}$ 250 °C	$\text{Log}C_{\text{ads}}$ 300 °C
$\text{CO}_{2\text{ads}}$	$\text{CO}_{2\text{ads}} + \text{H}_2\text{O} = \text{H}^+ + \text{HCO}_3^-$	-7.3403	-7.0983	-7.0033	-7.0973	-7.4013	-7.8483	-8.4203	-9.1573

$\text{Log}C_{\text{ads}}$  values follow the TOUGHREACT format, i.e., at eight different temperatures (0, 25, 60, 100, 150, 200, 250 and 300 °C) and pressures (1 bar from 0–100 °C, and after vapor pressure).

Since kinetic parameters for  $\text{CO}_{2\text{ads}}$  are not available, reaction at equilibrium condition was assumed.

### 3.3. Reaction-Diffusion Experiments Model

Diffusion coefficient ( $1.61 \times 10^{-10} \text{ m}^2/\text{s}$ ) for Reactive Transport Model (RTM) and specific reactive area of minerals (Table 2) were initially obtained by reaction-diffusion experiments (Figure 2) and laboratory analyses performed on core samples [39], respectively. Data were successively calibrated by a simplified numerical model, reproducing the experiments and considering  $\text{CO}_2$  adsorption and geochemical reactions. The 1D model, representing the rock specimen, is 0.55 cm long, fully saturated in pure water and discretized by a uniform grid of 100 cells (0.05 mm each one). An infinite boundary element of the same dimension, with  $\text{CO}_{2(\text{g})}$  saturation of 0.5 at in situ temperature for Seal 6, Seal 4 and reservoir samples (i.e., 75 °C, 105 °C, 415 °C and 140 °C, respectively) and 60 bar of  $\text{PCO}_2$ , was added at the left side of the domain, representing the part of the specimen in contact with  $\text{CO}_2$ -rich water. No flow was assigned to the right boundary of the domain. Simulations were performed with the modified version of TOUGHREACT (see Section 3.1) by using input data and parameters as above described.

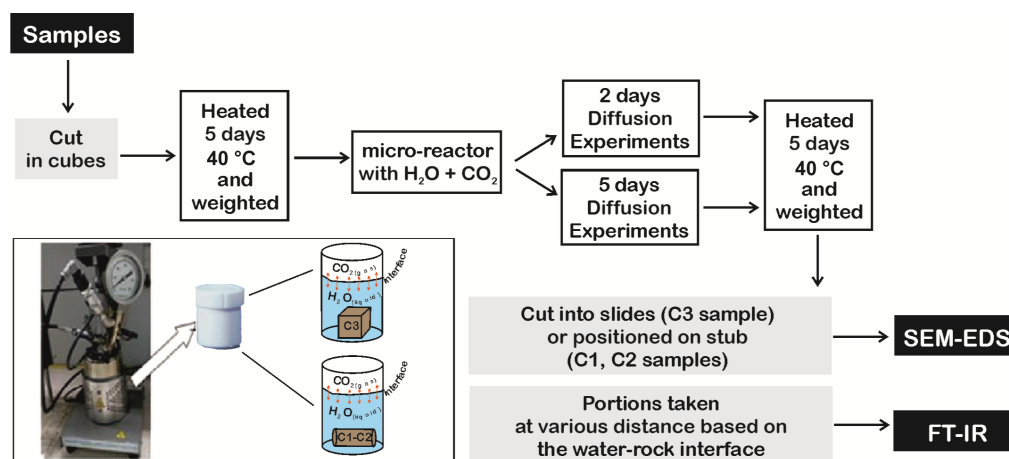


Figure 2. Workflow of diffusion experiments.

#### 4. Models Parameters

The numerical simulations were performed using both fluid flow and reactive transport models to evaluate the impact of CO<sub>2</sub> reactions on leakage pathways and timescales.

Existing 3D models of the area based on seismic and well log data analysis, which include geometries of the main horizons (i.e., seabed, Seal 6, Seal 4, top reservoir), faults nearby the reservoir and main petrophysical properties (bulk density, total and effective porosity, permeability, clay content), were provided by Petronas, with a vertical resolution of 20 m and a horizontal resolution of 200 m × 200 m. These data were used to build and populate the computational domains employed in the numerical simulations (see Section 5).

A heterogeneous porous medium was modeled by using provided 3D models of clay content, porosity and both vertical and horizontal permeability [59]. These data, with a resolution of 20 m, were mapped at the cells of the domain defining 15 different rock types based on the clay content values. In particular, each cell of the domain was classified in 7 classes: silt (<0.063 fraction volume of clay content); silty clay (0.063–0.142 fraction volume of clay content), and five shale rocks (clay1: 0.142–0.282; clay2: 0.282–0.422; clay3: 0.422–0.562; clay4: 0.562–0.702 and clay 5 > 0.702 fraction volume of clay content) both for Seal 6-soft sediments and Seal 4; whereas a rock type constituted by carbonates was defined for the reservoir. Porosity values range from 9 to 35% in the reservoir and from 20 to 33% in the Seal 4 and Seal 6. Permeability was set to  $1 \times 10^{-13} \text{ m}^2$  for the reservoir, whereas for the overburden three permeability models were created based on different approaches. Permeability Model A is generated from clay and porosity values after calibration with core lab analyses [59]; Model B assumes the same permeability distributions of Model A but imposes a fix value of 0.003 mD for the five shale rocks, in agreement to average permeability measurements in other wells in the investigated area (Petronas communication); Model C scaled down the permeability values of Model A by a factor of 100 in shale rock type. In all the permeability Models, horizontal permeability is always higher than vertical one, with an average ratio ranging from 0.16 to 0.88.

For each of the 15 rock types, specific heat capacity and thermal conductivity were indirectly defined as a function of thermal properties of all rock forming mineral phases with respect to their abundances as obtained by XRPD analysis [60–62]. The domain is fully saturated by water. Since Seal 6-soft sediments are in hydrostatic equilibrium with sea a NaCl mass fraction of 0.034 was assigned; whereas 0.02 NaCl mass fraction, corresponding to salinity of the reservoir (Petronas data), was used for Seal 4 and reservoir.

In the RTM model, initial mineralogical and aqueous composition was assigned for each of the 15 defined rock types. The solid phases were defined on the basis of core samples laboratory analysis (XRPD, XRF and SEM-EDS) [39] and recomputed to redistribute the average mineral percentage as a function of the clay content (Table 2). For soft sediments (top domain) the same mineral assemblage of Seal 6 was used, since no



laboratory information on this section of overburden is available, whereas for the reservoir the composition obtained by the corresponding rock sample was used. To accomplish the high Fe content in muscovite, Fe-Celadonite ( $\text{KFeAlSi}_4\text{O}_{10}(\text{OH})_2$ ) was used in the models instead of muscovite ( $\text{KAl}_2(\text{AlSi}_3)\text{O}_{10}(\text{OH})_2$ ) since it is the Fe-K end-member of muscovite-celadonite series.

Mineral assemblage already includes primary and potential secondary phases. Moreover, analysis and diffusion experiments show primary carbonate dissolution and weathering of pyrite to form secondary carbonates belonging to siderite-ankerite series. Therefore, no secondary minerals were added to the model.

In agreement with fluid flow conditions, a typical seawater composition (35 g/L) was used for Seal 6-soft sediments; whereas a 26 g/L NaCl equivalent water was used for Seal 4 and reservoir.

## 5. Leakage Scenarios

$\text{CO}_2$  leakage from the carbonate reservoir toward the seabed may occur for different processes over different timescales. Two scenarios were formulated; the Scenario 1 represents the leakage from the top of the reservoir in the overburden and the Scenario 2 supposes the leakage of  $\text{CO}_2$  throughout the F05 fault connecting the reservoir to seabed (Figure 1).

The domain geometry is derived from the interpolation of the layer interfaces on the computational grid. In the horizontal direction, the cell resolution is variable with a finer value (20 m) near the reservoir and the F05 fault, and coarser (200 m) at the outermost boundary. Vertical resolution is always 20 m. The lateral boundaries are far enough to prevent boundary conditions affecting the numerical solutions.

Dirichlet boundary conditions for pressure and temperature are assigned to the top boundary at the sea level and bottom boundary. Initial temperature and pressure of the model follow the geothermal and geobaric gradient estimated from wells data measurements. No flow conditions are assigned to the lateral boundaries.

A  $\text{CO}_2$  mass fraction of  $3.7 \times 10^{-5}$  is assigned to the cells of the domain which are outside the reservoir ( $\text{CO}_{2(\text{aq})}$  content of seawater).

The domain of Scenario 1 is constituted by a 3D axi-symmetric model using a section running from the center of the reservoir top along E-W direction for about 5 km (Figure 3a). The domain extends vertically from the sea bottom down to 2200 m (the depth of the current gas-water contact).

The distribution of permeability (Model C) is shown in Figure 3b. The gas cap was modeled as a  $\text{CO}_2$  gas bubble within the reservoir by assigning to its cells a gas saturation equal to one, a  $\text{CO}_2$  partial pressure of 25 MPa, i.e., corresponding to 70% of total pressure and a fixed temperature of 133 °C. Except for the cells within the reservoir, initial temperature and pressure of the model follow the geothermal and hydrostatic gradients of the area.

No flow boundary conditions assigned to the left lateral side of the domain warrant the symmetry condition of the flow along the axis of symmetry.

In the second scenario, we hypothesized the uprising of  $\text{CO}_2$  along the FO5 fault. The fault is about 3 km far from the edge of the reservoir and crosses the overburden up to 300 m depth (Figure 1b). The domain is constituted by a 2D model using a profile starting from the K5-3 well toward west for about 7 km (Figure 4a) and crossing the FO5 fault. Vertically, the profile extends from sea bottom down to -2800 m. The distribution of permeability Model C is shown in Figure 4d. The rock properties were mapped over a section defined by the E-W section and clearly show a dislocation across the FO5 fault. A damage zone of 300 m width (PETRONAS communication, Figure 4b) is estimated from seismic data and modeled around the FO5 fault. Values of 10 mD and 1 mD were assigned to the damage zone for permeability Models A and C, respectively, which are around 100 times higher than the shale permeability in the overburden rock formations. The permeability of the damage zone falls in the range of 1–10 mD reported in literature for fractured shales [63] and represents the worst possible scenario.

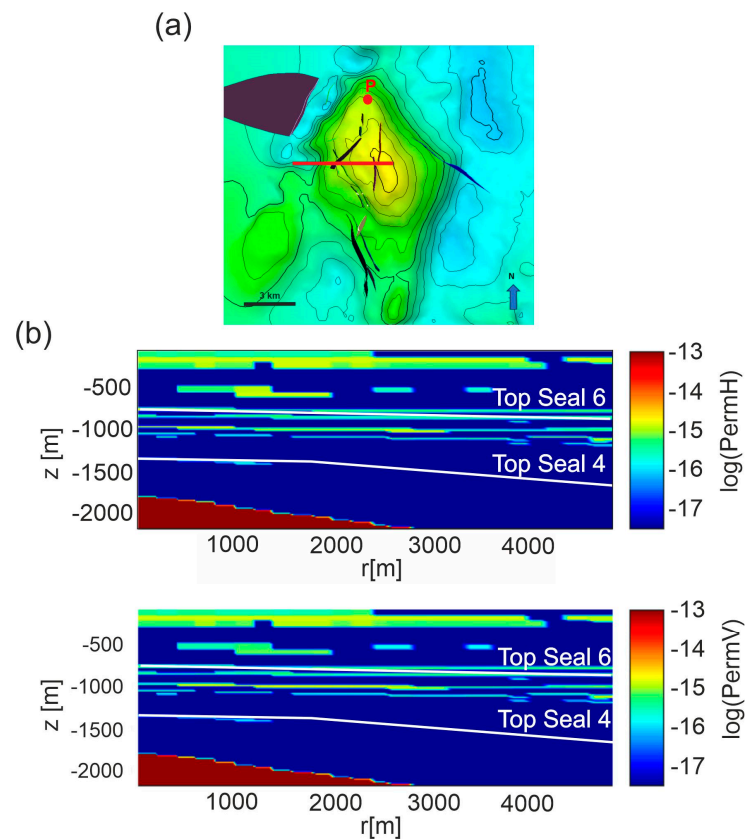


**Figure 3.** Scenario 1. (a) The E-W section (red line) running from the center of the reservoir top. Faults are represented as colored surfaces. (b) horizontal (permH) and vertical (permV) permeabilities distribution for Model C, interpolated on the computational domain derived for the section. Permeability Models A and B are shown in Figure S1 in Supplementary Material.

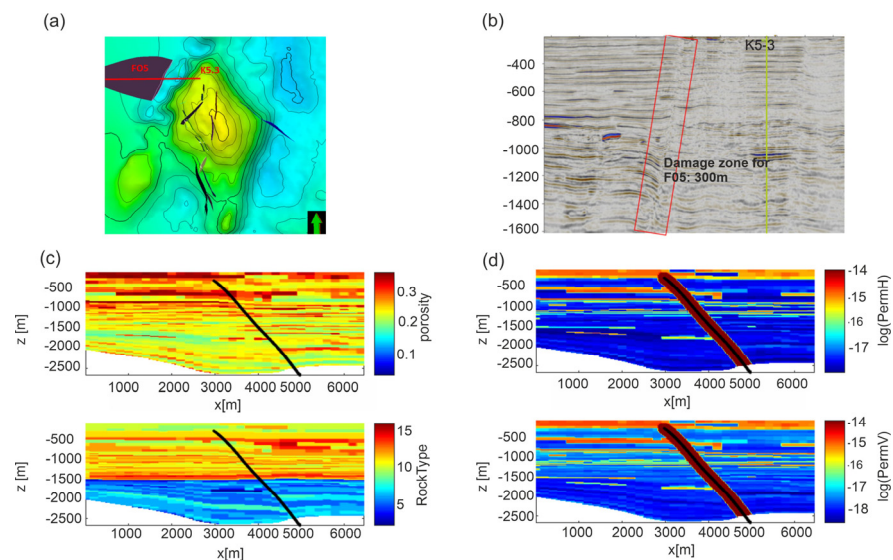


**Figure 4.** Scenario 2. (a) E-W section (red line) from the P well crossing the FO5 fault. Black lines are faults in the overburden not considered in the model. (b) Seismic section of the modeled structure. Note that the seismic section is reflected as if in a mirror with respect to the numerical domain of Scenario 2. (c) Distribution of porosity and rock type and (d) distributions of horizontal (permH) and vertical (permV) permeabilities for Model C in the computational domain. The P well is positioned on the left lateral boundary of the domain. The black line represents the FO5 fault. Permeability Model A is shown in Figure S2 in Supplementary Material.

The performed simulation in Scenario 2 assumes that the reservoir water phase, at the bottom of the domain, is saturated in  $\text{CO}_2$ , since its depth is below the gas water contact level (2200 m depth). On the cells belonging to the domain bottom, a mass fraction of 0.05 is assigned, which corresponds to the  $\text{CO}_2$  saturation at in situ condition (temperature, pressure and salinity) after equilibrium with carbonates (e.g., calcite). The  $\text{CO}_{2(\text{aq})}$  mass fraction is estimated using the solubility models of [64,65].

## 6. Results and Discussion

### 6.1. Scenario 1—Leakage from Reservoir

In Scenario 1, simulations were set up to reconstruct the pressure gradient measured in exploration wells and investigate the possible migration of  $\text{CO}_2$  from the top of the carbonate reservoir throughout the overburden.

In the fluid flow model, the numerical simulation outputs provide the distributions of gas saturation ( $S_g$ ) and  $\text{CO}_2$  mass fraction ( $X_{\text{CO}_2}$ ) in the liquid phase over time. Depending on the permeability model, after 10,000 years gaseous  $\text{CO}_2$  upraises at about  $-800$  m in permeability Model A (Figure S3),  $-1600$  m in Model B (Figure S4) and  $-1700$  m in permeability Model C (Figure 5a). The aqueous  $\text{CO}_2$  distribution has a similar behavior. After 300,000 years the  $X_{\text{CO}_2} = 0.04$  (i.e., 0.98 mol/L) reaches  $-800$  m in Model B (Figure S4) and  $-1300$  m in Model C (Figure 5b). As a consequence, the upward propagation velocity is faster for Model A (77 m/1000 y) than Models B and C (2 m/1000 y and 1 m/1000 y, respectively). Since Models A and C represent the two permeability end-members, hereafter only results of these two Models will be presented and discussed.

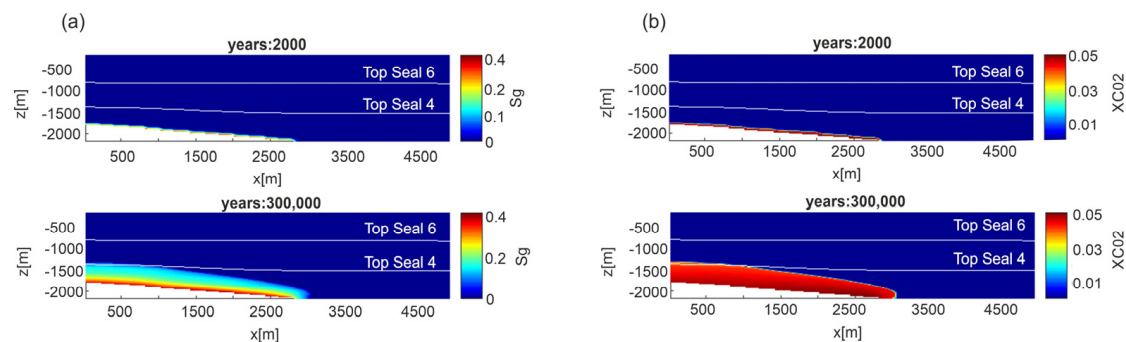


**Figure 5.** Scenario 1, E-W section, permeability Model C. Distribution of: (a) gas saturation ( $S_g$ ) and (b)  $\text{CO}_2$  mass fraction ( $X_{\text{CO}_2}$ ) in the liquid phase at two different time steps.

The comparison between the Darcy and diffusive flux (permeability Model C is reported in Figure 6, whereas Model A is shown in Figure S5) shows that the latter mainly contributed at the propagation front in low permeability systems, where the contribution of the diffusive flow becomes more important, owing to the higher  $\text{CO}_2$  concentration gradient.

The range of flow regimes in shales depends on the pore throat sizes and the pressures. Knudsen diffusion becomes important with pores on the order of a few micrometers and low pressures. Based on measured Klinkenberg slippage factor (0.07 MPa), the estimated Knudsen coefficient at reservoir/caprock condition is on the order of  $10^{-4}$ , which is in a range where the flow is mainly in the Darcy regime and hence Knudsen diffusion could be considered negligible [23].

In all permeability Models  $\text{CO}_2$  migrates mainly upward due to the buoyancy effect and no lateral propagation is observed. This may be due to the lack of lenses of high permeability rocks in the analyzed E-W section. Then, to examine if the presence of higher permeability lenses may favor lateral migrations, other sections were explored by inspecting the presence of well-developed and connected lenses with clay content lower than 0.142 fraction volume. Along a N-S section, running from the top of the reservoir toward North (Figure 7), a network of connected lenses at a depth of about 1400 m was found. Therefore, further simulations were performed by setting up a computational

domain along this section. Simulation results for permeability Models A and C show that notwithstanding the presence of connected horizontal higher permeability lenses, no lateral CO<sub>2</sub> migration is achieved (Figure 8 for Model C and Figure S7 for Model A) and both the uprising depth and velocity of CO<sub>2</sub> are very similar to those obtained along the E-W section. Moreover, the average vertical to horizontal permeability ratio in our system ranges from 0.16 to 0.88, so the two permeabilities are similar.

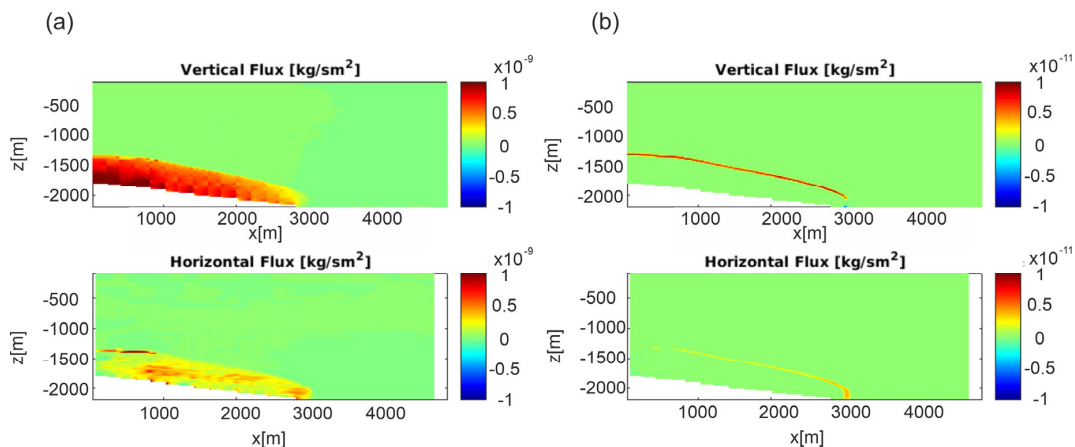


**Figure 6.** Scenario 1, E-W section, permeability Model C. (a) Darcy fluxes and (b) diffusive fluxes after 300,000 years.

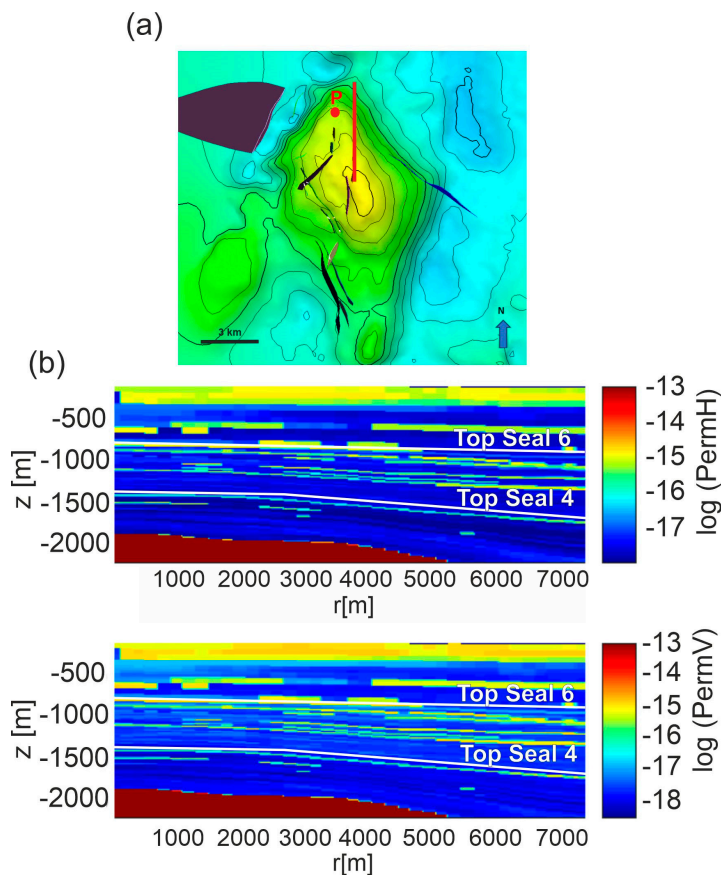


**Figure 7.** Scenario 1. (a) the N-S section (red line) running from the center of the reservoir top. (b) Horizontal (permH) and vertical (permV) permeabilities distribution for Model C interpolated on the computational domain derived for the section. Permeability Model A is shown in Figure S6 of Supplementary Material.



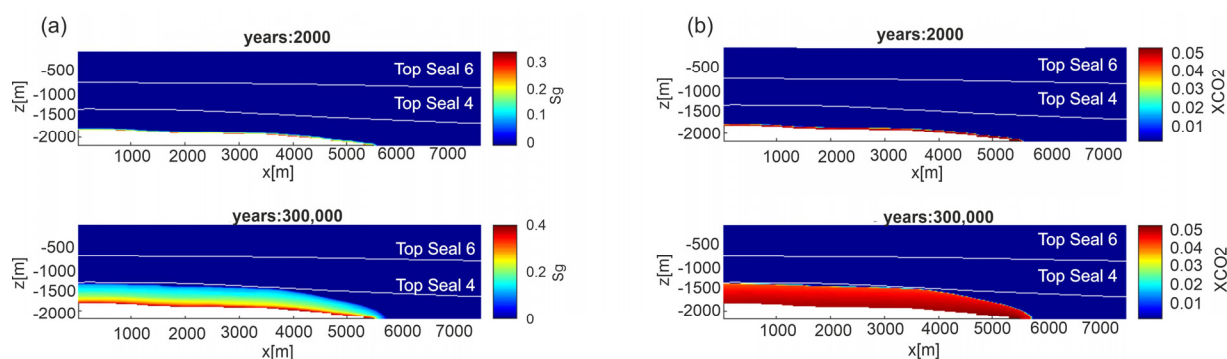


**Figure 8.** Scenario 1, N-S section, permeability Model C. Distribution of: (a) gas saturation ( $S_g$ ) and (b)  $\text{CO}_2$  mass fraction ( $X_{\text{CO}_2}$ ) in the liquid phase at two different time steps. Results for permeability Model A are shown in Figure S7 of Supplementary Material.

Ref. [66] investigated the  $\text{CO}_2$  migration in heterogeneous formations (alternating shale- and sand-rich layers), partially filled with oil and limited sealing capabilities, developing a sequestration strategy based on simultaneous multi reservoir layer injection. They suggested that injected  $\text{CO}_2$  spreads out laterally in small permeable layers driven by buoyancy. Where  $\text{CO}_2$ -brine capillary pressure exceeds the threshold pressure  $\text{CO}_2$  can move vertically according to a combination of lateral and vertical migration, until it is trapped by dispersion trapping.

Differently to what is proposed by [66], in our systems the permeability ratio (permV/permH) is not small enough to generate lateral leakages from the reservoir. Furthermore, we simulated migration from reservoirs and not simultaneous injection in sandy layers, which would have maximized lateral dispersion of  $\text{CO}_2$ . On the other hand, we cannot exclude the 20 m grid resolution may not be enough to reveal smaller lenses that might lead to lateral leakages. However, we found in the Seal 6 upper levels, hints of lateral migration after 300,000 y when considering permeability Model B (Figure S4 in Supplementary Material).

The preferential vertical migration in a heterogeneous system was modeled also by [67], for the Ketzin storage site. They found that with a permeability ratio of 0.33 the main migration process is the buoyancy and that to have a lateral migration a permV/permH ratio of 0.01 is needed.

Figure 9 shows the pore pressure profiles measured in the three wells and those computed by simulations for permeability Model C (results for permeability Model A are shown in Figure S8 of Supplementary Material) in both E-W and N-S sections at steady state conditions (after 300,000 years). Simulated results are in good agreement with field data, mirroring the gas migration and providing validation of the developed model for Scenario 1. Depending on the permeability Model and section, the depth of the overpressured area changes from 1300 m to 1500 m. The best fit is reached for permeability Model C along the N-S section. Over time the pore pressure propagates from the reservoir until the top of Seal 4, which therefore does not constitute an effective barrier to  $\text{CO}_2$  uprising.

In order to investigate the effect of geochemical reactions on  $\text{CO}_2$  migration, a reactive transport model was implemented. The addition of the chemistry in the model generates a little lower convergence with respect to pure fluid flow and gives a significant increase in the runtime. Then, to optimize computational time and considering the pressure profile results, only permeability Model C was investigated by RTM.

As expected, the RTM simulations show that the main reactions occur in the reservoir and at the reservoir-caprock interface.

Figure 10 shows carbonate weathering after 10,000 years. Calcite dissolves up to  $1 \times 10^{-4}$  vol.% in a restricted area in the upper part of the reservoir and along the reservoir-caprock interface (Figure 10a). Dolomite and siderite dissolution (up to  $1 \times 10^{-4}$  vol.% and  $8.6 \times 10^{-4}$  vol.%, respectively; Figure 10b,c) affects a wider portion of the reservoir from the top to almost the bottom of the domain. Consequently, porosity (Figure 10d) increases at the

reservoir-caprock interface (up to 0.054%). Kaolinite dissolves (up to  $-1.0 \times 10^{-4}$  vol.%; Figure 11b) in the reservoir and in Seal 4 and Seal 6, whereas it forms in soft sediments. Also pyrite slightly dissolves in the reservoir and in all the Seal 4, following the carbonate weathering zone, whereas it precipitates at the reservoir-caprock interface. Quartz little forms in the reservoir while it dissolves in the overburden.

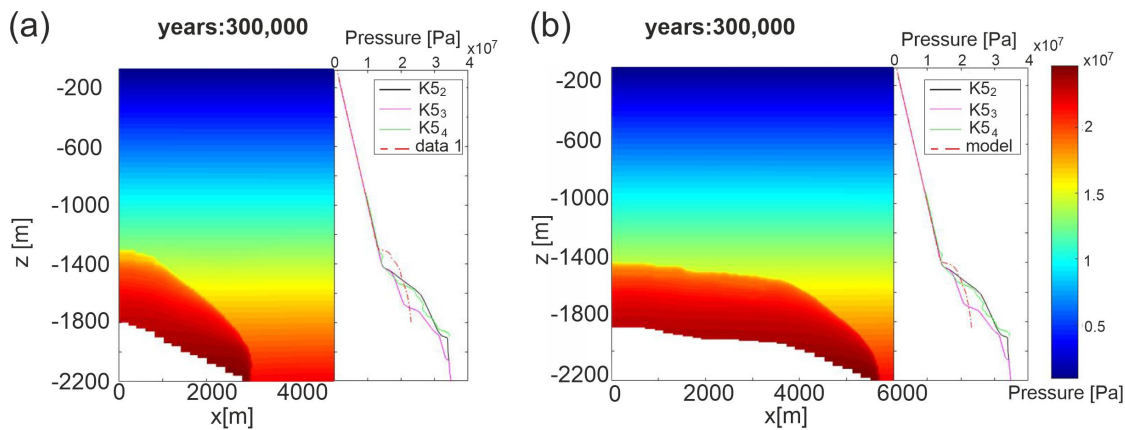


Figure 9. Scenario 1, permeability Model C, pore pressure profiles measured in the three wells with respect to simulated ones at steady state. (a) E-W section; (b) N-S section.

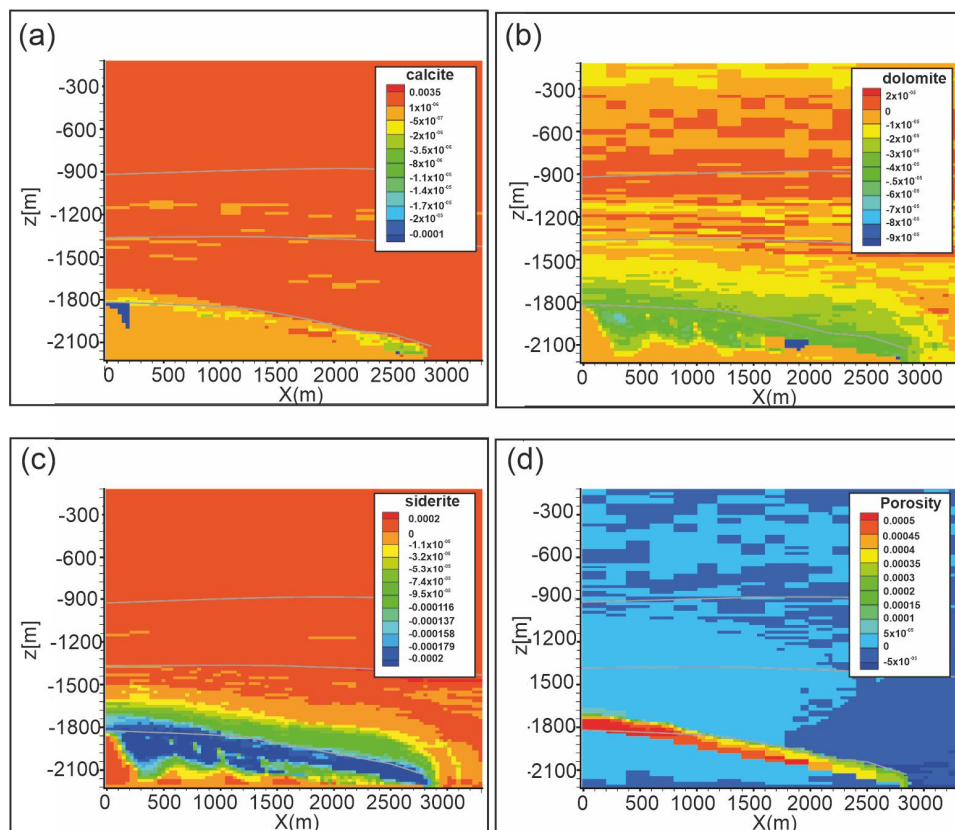
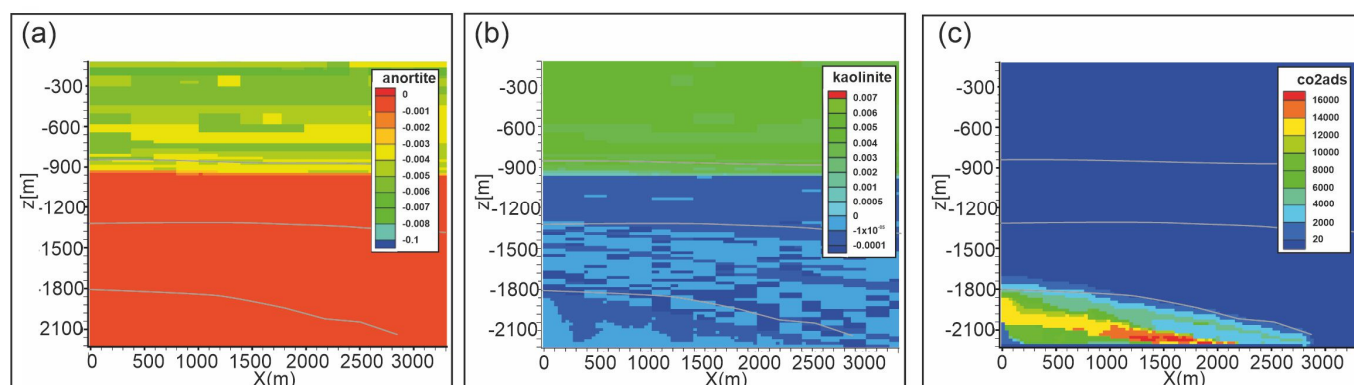


Figure 10. Scenario 1. Distribution of: (a) calcite abundance change (volume %), (b) dolomite abundance change (volume %), (c) siderite abundance change (volume %), (d) porosity change (fraction volume) after 10,000 y. Gray lines represent Seal 4, Seal 6 and reservoir horizons.



**Figure 11.** Scenario 1. Distribution of: (a) anorthite abundance change (volume %); (b) kaolinite abundance change (volume %); (c) adsorbed  $\text{CO}_2$  ( $\text{mol}/\text{m}^3$ ) after 10,000 years. Gray lines are Seal 4, Seal 6 and reservoir horizons.

A weathering zone develops also from the top of the reservoir penetrating into Seal 4 up to about 300 m with the dissolution of dolomite and siderite. At the reaction front, waters rich in salts, originated by mineral dissolution, move away from the  $\text{CO}_2$ -rich zone (e.g., back diffusion within the reservoir) mixing with “fresh” formation waters and allowing the precipitation of secondary minerals. This occurs for calcite and siderite which slightly form in the Seal 4. The extent of these reactions is moderate, since the pH in shale doesn’t fall below 6.7 (after 10,000 years) and the liquid phase becomes easily saturated in dissolved minerals reaching the equilibrium condition due to low flow velocity.

In the upper and intermediate part of the domain (i.e., Seal 6 and soft sediments), where  $\text{CO}_2$  is not present, some reactions occur, consisting of alteration of plagioclase (anorthite; Figure 11a) to produce kaolinite (Figure 11b) and carbonates. These reactions are mainly due to the fluid exchange between different lithotypes in close contact, e.g., sand-shale, that have formation waters composition different from each other.

Fe-illite, chlorite and Fe-celadonite remain quite stable in the whole domain for the all simulated time.

Adsorption of  $\text{CO}_2$  was modeled as a “fake” mineral at the equilibrium condition with zero initial concentration. After 10,000 years the  $\text{CO}_2$  is mainly adsorbed in the central portion of the reservoir (up to  $17,200 \text{ mol}/\text{m}^3$ ). The adsorbed  $\text{CO}_2$  distribution substantially follows the  $\text{CO}_2$  plume, penetrating in the caprock for about 50 m.

The computed  $\text{CO}_{2\text{ads}}$  is two orders of magnitude higher than that values obtained in laboratory experiments by e.g., [25,26,68] which found values ranging from 222 to  $470 \text{ mol}/\text{m}^3$ . This adsorption overestimation could be due to several factors, which are: (1) the maximum adsorption capacity of shales is not considered in our model and this leads to theoretically infinite adsorption capacity; (2) a general feature in  $\text{CO}_2$  adsorption isotherms is a continuous decline after a maximum value [26,68]. This declining part of the isotherms occur at high pressures ( $>9 \text{ MPa}$ ; Busch et al., 2008) which has been attributed to a volumetric effect (volume of the sorbed phase, sample swelling; [69]) not reported in the results of [57] from which we computed the  $\text{Log}C_{\text{ads}}$ ; (3) the clays used in [57] experiments could have some textural differences from the shales considered in this study, affecting the properties of sorbent phases and their surface parameters. The scarcity of  $\text{CO}_{2\text{ads}}$  data obtained in different formations and the fact that most of experimental data are measured at laboratory or at lower temperatures ( $25\text{--}50 \text{ }^\circ\text{C}$ ) with respect to those of our system, create large uncertainties and are likely the reasons for the high adsorption values we obtained from our simulations compared to other works. Indeed, according to [70] the  $\text{CO}_2$  adsorption capacity increases with temperature.

## 6.2. Scenario 2—Leakage from Faults

In this scenario, the uprising of CO<sub>2</sub> along the FO5 fault was investigated. Based on the simulation results of Scenario 1, CO<sub>2</sub> migrates almost upward from the reservoir without any significant lateral propagation. Therefore, we neglected the possibility that CO<sub>2</sub> leakage from caprock may laterally reach the FO5 fault and then propagate upward through the fault and directly simulated the uprising from the reservoir.

Results for gas saturation and CO<sub>2</sub> mass fraction in the liquid phase for fluid flow simulations are reported in Figure 12, for permeability model C (results for permeability Model A, are shown in Figure S9 in Supplementary Material). The CO<sub>2</sub> rises through the damage zone of the FO5 fault, due to the higher permeability with respect to the surrounding rocks. The rising velocity is obviously controlled by the permeability model. Dissolved CO<sub>2</sub> reaches a depth of about 800 m in 4000 years for Model C and the same depth in 500 years for Model A. The different pressure between the top reservoir, where solubility of CO<sub>2</sub> is controlled by gas over-pressure, and the fault, which has a hydrostatic pressure, leads to the formation of CO<sub>2</sub> bubbles. Over time, bubbles form and slowly rise within the damage zone reaching a depth of about −1500 in 4000 years for Model C and −1500 m in 500 years for Model A. The CO<sub>2</sub> distribution shows the presence of liquid and gas phases within the damage zone of the FO5 fault. This phenomenon is visible by the seismic attenuation observed in the seismic section (Figure 4b), confirming also for this scenario the validity of developed model to reproduce the investigated system. No CO<sub>2</sub> lateral flow, throughout more permeable lenses, is recognized from the damage zone to the overburden.

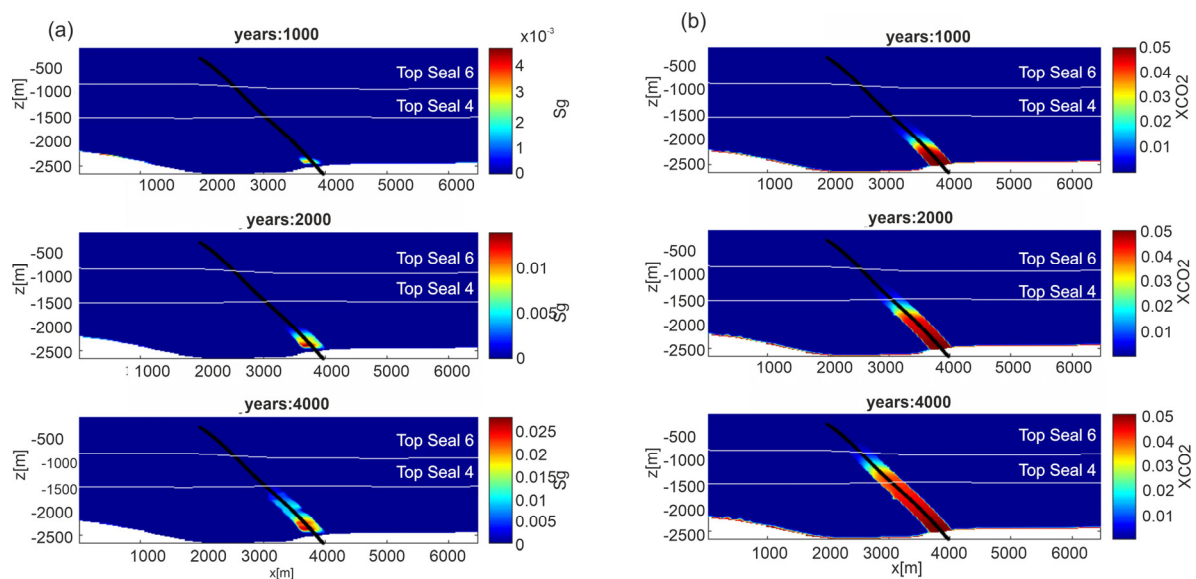


**Figure 12.** Scenario 2, permeability model C. Distribution of: (a) gas saturation ( $S_g$ ) and (b) CO<sub>2</sub> mass fraction in the aqueous phase ( $X_{CO_2}$ ) from depth through fault FO5, at three different time steps (1000, 2000 and 4000 years). Results for permeability Model A are shown in Figure S9 in Supplementary Material.

To reduce the computation effort, RTM simulation was carried out for a period of 1000 years. Over this time, the CO<sub>2(aq)</sub> present at the fault bottom enters in the damage zone, rises up to the bubble point and forms a gas phase, without substantially differences from the fluid flow model. As occurred for Scenario 1, the main reactions regard carbonates and adsorbed CO<sub>2</sub> around the fault (over 1000 mol/m<sup>3</sup>). Dolomite (not shown) minimally dissolves ( $-1.5 \times 10^{-5}$  vol.%) inside the damage zone whereas calcite ( $1.6 \times 10^{-5}$  vol.%) and siderite ( $1 \times 10^{-4}$  vol.%) precipitate (Figure 13). The precipitation of carbonates (carbonation process) in fractures and faults is a very common phenomenon which is favored by the exsolution of CO<sub>2</sub> along the rising flow-path. Also pyrite slightly forms ( $5 \times 10^{-6}$  mol/L) in the lower part of the fault, where highest CO<sub>2(aq)</sub> concentrations are present (Figure 13d). Among silicate minerals, kaolinite slightly dissolves ( $-1.25 \times 10^{-5}$  vol.%) inside the dam-



age zone, whereas it precipitates in the soft sediments ( $1.9 \times 10^{-3}$  vol.%) due to anorthite dissolution ( $-1 \times 10^{-3}$  vol.%). Kaolinite dissolves also in the Seal 4 and Seal 6, mirroring the rock type distribution (Figure 4c).

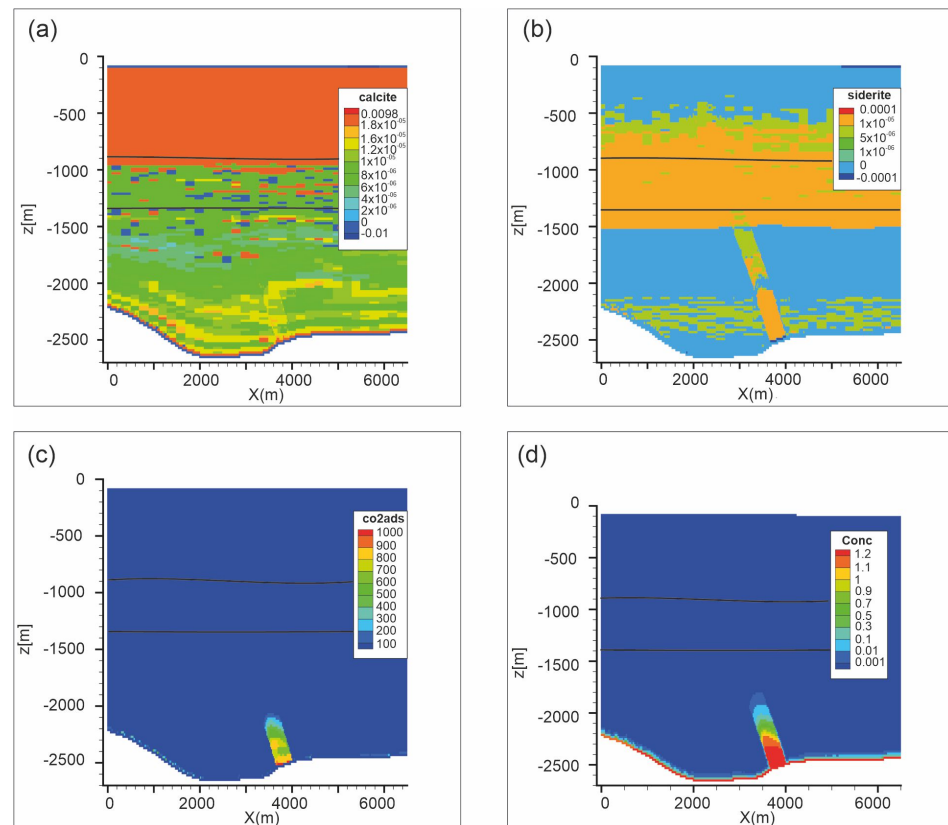


**Figure 13.** Scenario 2. Distribution of (a) calcite abundance change (volume %); (b) siderite abundance change (volume %); (c) adsorbed  $\text{CO}_2$  ( $\text{mol}/\text{m}^3$ ) and (d) dissolved  $\text{CO}_2$  ( $\text{mol}/\text{L}$ ) after 1000 years. Black lines are Seal 4 and Seal 6 horizons.

Other carbonates and silicate reactions in the overburden, not directly related to  $\text{CO}_2$  interaction, can be ascribed to reactions between different lithotypes in close contact, e.g., sand-shale, that have different formation waters composition. Reactions in soft sediments are mainly due to the presence of marine water filling the sediments. Indeed, seawater composition favors clays formation as a result of the submarine weathering of feldspars [71].

After 1000 years of simulation, all other primary minerals (i.e., quartz, Fe-celadonite, Fe-illite and chlorite) remain stable along the fault path and in the overburden.

The adsorption of  $\text{CO}_2$  (Figure 13c) is localized in the damage zone and it is directly related to  $\text{CO}_{2(\text{aq})}$  concentration (Figure 13d). Also for this scenario adsorbed  $\text{CO}_2$  (up to  $1190 \text{ mol}/\text{m}^3$ ) is one order of magnitude higher than other studies [25,26,68]. The possible reasons have been already discussed above.

## 7. Conclusions

In this study, we developed a complex heterogeneous model, built on the basis of 3D real lithology, porosity and permeability distributions belonging to a deep structure in off-shore Malaysia basin. Two  $\text{CO}_2$  leakage scenarios from a carbonate reservoir throughout a shaly overburden were simulated by fluid flow and reactive transport, focusing on factors affecting  $\text{CO}_2$  migration, such as permeability, Knudsen effect, Fickian diffusion, geochemical reaction and  $\text{CO}_2$  sorption on clays.

In all considered scenarios the permeability distribution has the main impact on  $\text{CO}_2$  uprising velocity and pathways. Despite the analysis of various sections and the presence of

higher permeability lenses in the overburden, CO<sub>2</sub> upward migration is driven by buoyancy, and no lateral propagation is observed. This is also due to comparable values of permV and permH. This evidence ruled out the possibility that CO<sub>2</sub> leaked from the reservoir may migrate laterally toward the FO5 fault and reach the seabed, as initially supposed.

Results of Scenario 1, well reflected the pressure profile recorded in the explorations wells, reproducing the overpressured zone below the top of Seal 4 and confirming the suspected uprising of CO<sub>2</sub> from the reservoir to the Seal 4 top. The CO<sub>2</sub> migration in the low permeability Seal 4 is mainly due to the Darcy flow with a minor contribution of diffusive flow at the Seal 4–Seal 6 interface, where the CO<sub>2</sub> concentration gradient is higher. Although the small dimension of the pore throats of overburden shales, estimated Knudsen diffusion number is low (<0.001), and the flow regime follows the ideal Darcy's regime.

When geochemistry is included in the model, mainly carbonate reactions were observed. Reactions are limited due to both the low mobility of fluid phase and the initial mineral assemblage already containing all the CO<sub>2</sub>-induced alteration phases, such as carbonates and clays. Dissolution of carbonates and pyrite at the reservoir interface slightly increase porosity. The weathering zone penetrated also into Seal 4 following the CO<sub>2(aq)</sub> distribution.

In the leakage from the FO5 fault Scenario, CO<sub>2</sub> upraised from the reservoir along the damage zone. Due to the different pressure between fault and reservoir, a CO<sub>2</sub> bi-phase zone developed, leading to the formation of CO<sub>2</sub> bubbles. The CO<sub>2</sub> exsolution favored siderite and minor calcite precipitation inside the damage zone, reducing porosity and contributing to seal the fault. In zones where the damage zone is intersected by higher permeability horizontal lenses, no significant lateral leakages are observed and the CO<sub>2</sub> flow was confined within the fault zone. The seismic attenuation observed in the seismic section along the fault confirms the presence of fluid in the damage zone, validating the simulated results.

In all considered scenarios CO<sub>2</sub> adsorption on shales together with dissolved CO<sub>2</sub> represent the main trapping mechanisms. Modeled adsorbed CO<sub>2</sub> is about two orders of magnitude higher than reported values in the literature. This is likely due to the lack of a maximum adsorption limit of CO<sub>2</sub> in the shales and to the reducing adsorption capacity for pressures higher than 9 MPa, which are both not considered in our model. Moreover, the higher simulated temperatures with respect to laboratory experiments and the textural differences from our core samples and other shales could be the reason for the adsorption overestimation.

This study tried to reach the ambitious goal to improve the understanding of the effects of key phenomena on fluid flow throughout shales. Despite some assumptions and estimations of missing parameters, the developed model effectively captures the real processes of the investigated system as proved by the comparison with available pressure and seismic data. It can be easily exported to other sites potentially suitable for CO<sub>2</sub> geological storage.

**Supplementary Materials:** The following supporting information can be downloaded at: <https://www.mdpi.com/article/10.3390/min13081016/s1>, Figure S1: Scenario 1. Permeability distribution in Models A and B along the E-W section; Figure S2: Scenario 2. permeability distribution in Model A along the E-W section; Figure S3: Scenario 1, E-W section, permeability Model A. Gas saturation and CO<sub>2</sub> mass fraction distribution over time; Figure S4: Scenario 1, E-W section, permeability Model B. Gas saturation and CO<sub>2</sub> mass fraction distribution over time; Figure S5: Scenario 1, E-W section, permeability Model A. Darcy fluxes and diffusive fluxes after 300,000 years; Figure S6: Scenario 1. The N-S section and permeabilities distribution for Model A; Figure S7: Scenario 1, N-S section, permeability Model A. Distribution of gas saturation and CO<sub>2</sub> mass fraction in the liquid phase at different time steps; Figure S8: Scenario 1, permeability Model A. Pore pressure distribution measured in the three wells with respect to simulated ones at steady state; Figure S9: Scenario 2, permeability Model A. Distribution of gas saturation and CO<sub>2</sub> mass fraction in the liquid phase at different time steps.

**Author Contributions:** Conceptualization, G.C., B.C., G.M., R.N., M.S.M., Z.A.A.B., M.R.A.R. and Z.Z.T.H.; methodology, G.C., B.C., G.M., R.N., Z.A.A.B., M.R.A.R. and Z.Z.T.H.; software, G.C. and G.M.; validation, G.C., G.M. and B.C.; investigation, G.C., B.C., G.M., R.N., M.S.M., Z.A.A.B., M.R.A.R. and Z.Z.T.H.; resources, M.S.M., Z.A.A.B. and M.R.A.R.; data curation, G.C., G.M., B.C., R.N. and Z.Z.T.H.; writing—original draft preparation, G.C., B.C., R.N. and G.M.; writing—review and editing,

G.C., B.C., R.N. and G.M.; project administration, N.H.S.B. and N.H.; funding acquisition, M.S.M., M.R.A.R. and Z.A.A.B. All authors have read and agreed to the published version of the manuscript.

**Funding:** This research was funded by PETRONAS Research Sdn. Bhd. for the Project “Methodology of Mitigation CO<sub>2</sub> Leakages (Overburden Study).”

**Data Availability Statement:** The data presented in this study are available on request from the corresponding author.

**Acknowledgments:** The authors thank PETRONAS Research Sdn. Bhd. for the cooperation and help in this work. The authors gratefully acknowledge the Editor and the four anonymous reviewers which helped improve the manuscript.

**Conflicts of Interest:** The authors declare no conflict of interest.

## References

- Metz, B. *Carbon Dioxide Capture and Storage: Special Report of the Intergovernmental Panel on Climate Change*; Cambridge University Press: Cambridge, UK, 2005.
- Metz, B.; Davidson, O.R.; Bosh, P.R.; Dave, R.; Meyer, L.A. *Contribution of Working Group III to the Fourth Assessment Report of the Intergovernmental Panel on Climate Change, 2007*; Cambridge University Press: Cambridge, UK; New York, NY, USA, 2007.
- IPCC. *2013 Revised Supplementary Methods and Good Practice Guidance Arising from the Kyoto Protocol*; IPCC: Geneva, Switzerland, 2014; ISBN 978-92-9169-140-1.
- IEA. *Greenhouse Gas R&D Programme Natural and Industrial Analogues for Geological Storage of Carbon Dioxide*; IEA Greenhouse Gas R&D Programme: Cheltenham, UK, 2009.
- Celia, M.A.; Nordbotten, J.M.; Bachu, S.; Dobossy, M.; Court, B. Risk of Leakage versus Depth of Injection in Geological Storage. *Energy Procedia* **2009**, *1*, 2573–2580. [[CrossRef](#)]
- Imbus, S.W.; Dodds, K.; Otto, C.J.; Trautz, R.C.; Christopher, C.A.; Agarwal, A.; Benson, S.M. CO<sub>2</sub> Storage Contingencies Initiative: Detection, Intervention and Remediation of Unexpected CO<sub>2</sub> Migration. *Energy Procedia* **2013**, *37*, 7802–7814. [[CrossRef](#)]
- Gholami, R.; Raza, A.; Iglauer, S. Leakage Risk Assessment of a CO<sub>2</sub> Storage Site: A Review. *Earth-Sci. Rev.* **2021**, *223*, 103849. [[CrossRef](#)]
- Gaus, I. Role and Impact of CO<sub>2</sub>–Rock Interactions during CO<sub>2</sub> Storage in Sedimentary Rocks. *Int. J. Greenh. Gas Control* **2010**, *4*, 73–89. [[CrossRef](#)]
- Esposito, A.; Benson, S.M. Evaluation and Development of Options for Remediation of CO<sub>2</sub> Leakage into Groundwater Aquifers from Geologic Carbon Storage. *Int. J. Greenh. Gas Control* **2012**, *7*, 62–73. [[CrossRef](#)]
- Vialle, S.; Druhan, J.L.; Maher, K. Multi-Phase Flow Simulation of CO<sub>2</sub> Leakage through a Fractured Caprock in Response to Mitigation Strategies. *Int. J. Greenh. Gas Control* **2016**, *44*, 11–25. [[CrossRef](#)]
- Brunet, J.-P.L.; Li, L.; Karpyn, Z.T.; Huerta, N.J. Fracture Opening or Self-Sealing: Critical Residence Time as a Unifying Parameter for Cement–CO<sub>2</sub>–Brine Interactions. *Int. J. Greenh. Gas Control* **2016**, *47*, 25–37. [[CrossRef](#)]
- Zhang, M.; Bachu, S. Review of Integrity of Existing Wells in Relation to CO<sub>2</sub> Geological Storage: What Do We Know? *Int. J. Greenh. Gas Control* **2011**, *5*, 826–840. [[CrossRef](#)]
- Ingram, G.M.; Urai, J.L.; Naylor, M.A. Sealing Processes and Top Seal Assessment. In *Norwegian Petroleum Society Special Publications*; Elsevier: Amsterdam, The Netherlands, 1997; Volume 7, pp. 165–174. ISBN 978-0-444-82825-5.
- Watts, N.L. Theoretical Aspects of Cap-Rock and Fault Seals for Single- and Two-Phase Hydrocarbon Columns. *Mar. Pet. Geol.* **1987**, *4*, 274–307. [[CrossRef](#)]
- Almutairi, A.; Al-Bazali, T. Capillary Pressure Behavior of CO<sub>2</sub>–Shale System at Elevated Temperatures. *Int. Res. J. Pure Appl. Chem.* **2022**, *23*, 1–16. [[CrossRef](#)]
- Hemme, C.; Van Berk, W. Change in Cap Rock Porosity Triggered by Pressure and Temperature Dependent CO<sub>2</sub>–Water–Rock Interactions in CO<sub>2</sub> Storage Systems. *Petroleum* **2017**, *3*, 96–108. [[CrossRef](#)]
- Zhang, L.; Wang, Y.; Miao, X.; Gan, M.; Li, X. Geochemistry in Geologic CO<sub>2</sub> Utilization and Storage: A Brief Review. *Adv. Geo-Energ. Res.* **2019**, *3*, 304–313. [[CrossRef](#)]
- Xu, T.; Pruess, K. Modeling multiphase non-isothermal fluid flow and reactive geochemical transport in variably saturated fractured rocks: 1. *Methodology* **2001**, *301*, 16–33. [[CrossRef](#)]
- Xu, T.; Sonnenthal, E.; Spycher, N.; Pruess, K. TOUGHREACT—A Simulation Program for Non-Isothermal Multiphase Reactive Geochemical Transport in Variably Saturated Geologic Media: Applications to Geothermal Injectivity and CO<sub>2</sub> Geological Sequestration. *Comput. Geosci.* **2006**, *32*, 145–165. [[CrossRef](#)]
- Soltanian, M.R.; Hajirezaie, S.; Hosseini, S.A.; Dashtian, H.; Amooie, M.A.; Meyal, A.; Ershadnia, R.; Ampomah, W.; Islam, A.; Zhang, X. Multicomponent Reactive Transport of Carbon Dioxide in Fluvial Heterogeneous Aquifers. *J. Nat. Gas Sci. Eng.* **2019**, *65*, 212–223. [[CrossRef](#)]
- Ershadnia, R.; Wallace, C.D.; Soltanian, M.R. CO<sub>2</sub> Geological Sequestration in Heterogeneous Binary Media: Effects of Geological and Operational Conditions. *Adv. Geo-Energy Res.* **2020**, *4*, 392–405. [[CrossRef](#)]

22. Yin, Y.; Qu, Z.; Prodanović, M.; Landry, C.J. Identifying the Dominant Transport Mechanism in Single Nanoscale Pores and 3D Nanoporous Media. *Fundam. Res.* **2023**, *3*, 409–421. [[CrossRef](#)]
23. Freeman, C.M.; Moridis, G.J.; Blasingame, T.A. A Numerical Study of Microscale Flow Behavior in Tight Gas and Shale Gas Reservoir Systems. *Transp. Porous Media* **2011**, *90*, 253–268. [[CrossRef](#)]
24. Civan, F. Modeling transport in porous media by control volume analysis. *J. Por. Media* **2010**, *13*, 855–873. [[CrossRef](#)]
25. Khosrokhavar, R.; Griffiths, S.; Wolf, K.H. Shale Gas Formations and Their Potential for Carbon Storage: Opportunities and Outlook. *Environ. Process.* **2014**, *1*, 595–611. [[CrossRef](#)]
26. Busch, A.; Alles, S.; Gensterblum, Y.; Prinz, D.; Dewhurst, D.N.; Raven, M.D.; Stanjek, H.; Krooss, B.M. Carbon Dioxide Storage Potential of Shales. *Int. J. Greenh. Gas Control* **2008**, *2*, 297–308. [[CrossRef](#)]
27. Trevisan, L.; Krishnamurthy, P.G.; Meckel, T.A. Impact of 3D Capillary Heterogeneity and Bedform Architecture at the Sub-Meter Scale on CO<sub>2</sub> Saturation for Buoyant Flow in Clastic Aquifers. *Int. J. Greenh. Gas Control* **2017**, *56*, 237–249. [[CrossRef](#)]
28. Li, B.; Benson, S.M. Influence of Small-Scale Heterogeneity on Upward CO<sub>2</sub> Plume Migration in Storage Aquifers. *Adv. Water Resour.* **2015**, *83*, 389–404. [[CrossRef](#)]
29. Saadatpour, E.; Bryant, S.L.; Sepehrnoori, K. New Trapping Mechanism in Carbon Sequestration. *Transp. Porous Media* **2010**, *82*, 3–17. [[CrossRef](#)]
30. Nghiem, L.; Yang, C.; Shrivastava, V.; Kohse, B.; Hassam, M.; Card, C. Risk Mitigation through the Optimization of Residual Gas and Solubility Trapping for CO<sub>2</sub> Storage in Saline Aquifers. *Energy Procedia* **2009**, *1*, 3015–3022. [[CrossRef](#)]
31. Gaus, I.; Audigane, P.; André, L.; Lions, J.; Jacquemet, N.; Durst, P.; Czernichowski-Lauriol, I.; Azaroual, M. Geochemical and Solute Transport Modelling for CO<sub>2</sub> Storage, What to Expect from It? *Int. J. Greenh. Gas Control* **2008**, *2*, 605–625. [[CrossRef](#)]
32. Wang, J.; Luo, H.; Liu, H.; Cao, F.; Li, Z.; Sepehrnoori, K. An Integrative Model to Simulate Gas Transport and Production Coupled with Gas Adsorption, Non-Darcy Flow, Surface Diffusion, and Stress Dependence in Organic-Shale Reservoirs. *SPE J.* **2017**, *22*, 244–264. [[CrossRef](#)]
33. Vahrenkamp, V.C. Miocene Carbonates of the Luconia Province, Offshore Sarawak: Implications for Regional Geology and Reservoir Properties from Strontium-Isotope Stratigraphy. *BGSM* **1998**, *42*, 1–13. [[CrossRef](#)]
34. Ting, K.K.; Chung, E.; Al Jaaidi, O. *Evolution and Controlling Factors of Miocene Carbonate Build-up in Central Luconia, SE Asia: Insights from Integration of Geological and Seismic Characterization*; ICIPEG: Kuala Lumpur, Malaysia, 2010.
35. Madon, M.; Kim, C.L.; Wong, R. The Structure and Stratigraphy of Deepwater Sarawak, Malaysia: Implications for Tectonic Evolution. *J. Asian Earth Sci.* **2013**, *76*, 312–333. [[CrossRef](#)]
36. Janjuhah, H.T.; Salim, A.M.A.; Shah, M.M.; Ghosh, D.; Alansari, A. Quantitative Interpretation of Carbonate Reservoir Rock Using Wireline Logs: A Case Study from Central Luconia, Offshore Sarawak, Malaysia. *Carbonates Evaporites* **2017**, *32*, 591–607. [[CrossRef](#)]
37. Rankey, E.C.; Schlaich, M.; Mokhtar, S.; Ghon, G.; Ali, S.H.; Poppelreiter, M. Seismic Architecture of a Miocene Isolated Carbonate Platform and Associated Off-Platform Strata (Central Luconia Province, Offshore Malaysia). *Mar. Pet. Geol.* **2019**, *102*, 477–495. [[CrossRef](#)]
38. Ho, K.F. Stratigraphic Framework for Oil Exploration in Sarawak. *Bull. Geol. Soc. Malays.* **1978**, *10*, 1–13. [[CrossRef](#)]
39. Montegrossi, G.; Cantucci, B.; Piochi, M.; Fusi, L.; Misnan, M.S.; Rashidi, M.R.A.; Abu Bakar, Z.A.; Tuan Harith, Z.Z.; Bahri, N.H.S.; Hashim, N. CO<sub>2</sub> Reaction-Diffusion Experiments in Shales and Carbonates. *Minerals* **2022**, *13*, 56. [[CrossRef](#)]
40. Mualem, Y. A New Model for Predicting the Hydraulic Conductivity of Unsaturated Porous Media. *Water Resour. Res.* **1976**, *12*, 513–522. [[CrossRef](#)]
41. van Genuchten, M.T. A Closed-Form Equation for Predicting the Hydraulic Conductivity of Unsaturated Soils. *Soil Sci. Soc. Am. J.* **1980**, *44*, 892–898. [[CrossRef](#)]
42. Comisky, J.T.; Newsham, K.E.; Rushing, J.A.; Blasingame, T.A. A Comparative Study of Capillary-Pressure-Based Empirical Models for Estimating Absolute Permeability in Tight Gas Sands. *Proc. SPE Annu. Tech. Conf. Exhib.* **2007**, *3*, 1821–1838. [[CrossRef](#)]
43. Kampman, N.; Busch, A.; Bertier, P.; Snippe, J.; Hangx, S.; Pipich, V.; Di, Z.; Rother, G.; Harrington, J.F.; Evans, J.P.; et al. Observational Evidence Confirms Modelling of the Long-Term Integrity of CO<sub>2</sub>-Reservoir Caprocks. *Nat. Commun.* **2016**, *7*, 12268. [[CrossRef](#)]
44. Klinkenberg, L.J. The Permeability of Porous Media to Liquids and Gases. *Drill. Prod. Pract. Am. Pet. Inst.* **1941**, 200–213. [[CrossRef](#)]
45. Spycher, N.; Pruess, K.; Ennis-King, J. CO<sub>2</sub>-H<sub>2</sub>O Mixtures in the Geological Sequestration of CO<sub>2</sub>. I. Assessment and Calculation of Mutual Solubilities from 12 to 100 °C and up to 600 Bar. *Geochim. Cosmochim. Acta* **2003**, *67*, 3015–3031. [[CrossRef](#)]
46. Spycher, N.; Pruess, K. CO<sub>2</sub>-H<sub>2</sub>O Mixtures in the Geological Sequestration of CO<sub>2</sub>. II. Partitioning in Chloride Brines at 12–100 °C and up to 600 Bar. *Geochim. Cosmochim. Acta* **2005**, *69*, 3309–3320. [[CrossRef](#)]
47. Spycher, N.; Pruess, K. A Phase-Partitioning Model for CO<sub>2</sub>-Brine Mixtures at Elevated Temperatures and Pressures: Application to CO<sub>2</sub>-Enhanced Geothermal Systems. *Transp. Porous Media* **2010**, *82*, 173–196. [[CrossRef](#)]
48. Pan, L.; Spycher, N.; Doughty, C.; Pruess, K. *ECO<sub>2</sub>N V. 2.0: A New TOUGH2 Fluid Property Module for Mixtures of Water, NaCl, and CO<sub>2</sub>*; Lawrence Berkeley National Laboratory: Berkeley, CA, USA, 2014; p. 112.
49. Lasaga, A.C. Chemical Kinetics of Water-Rock Interactions. *J. Geophys. Res.* **1984**, *89*, 4009–4025. [[CrossRef](#)]
50. Lasaga, A.C.; Soler, J.M.; Ganor, J.; Burch, T.E.; Nagy, K.L. Chemical Weathering Rate Laws and Global Geochemical Cycles. *Geochim. Cosmochim. Acta* **1994**, *58*, 2361–2386. [[CrossRef](#)]



51. Steefel, C.I.; Lasaga, A.C. A Coupled Model for Transport of Multiple Chemical Species and Kinetic Precipitation/Dissolution Reactions with Application to Reactive Flow in Single Phase Hydrothermal Systems. *Am. J. Sci.* **1994**, *294*, 529. [[CrossRef](#)]
52. Palandri, J.L.; Kharaka, Y.K. *A Compilation of Rate Parameters of Water-Mineral Interaction Kinetics for Application to Geochemical Modeling*; U.S. Geological Survey: Reston, VA, USA, 2004.
53. Marini, L. *Geological Sequestration of Carbon Dioxide, Volume 11: Thermodynamics, Kinetics, and Reaction Path Modeling*; Elsevier: Burlington, ON, Canada, 2006; ISBN 978-0-08-046688-0.
54. Pokrovsky, O.S.; Golubev, S.V.; Schott, J.; Castillo, A. Calcite, Dolomite and Magnesite Dissolution Kinetics in Aqueous Solutions at Acid to Circumneutral PH, 25 to 150 °C and 1 to 55 Atm PCO<sub>2</sub>: New Constraints on CO<sub>2</sub> Sequestration in Sedimentary Basins. *Chem. Geol.* **2009**, *265*, 20–32. [[CrossRef](#)]
55. Blanc, P.; Lassin, A.; Piantone, P.; Azaroual, M.; Jacquemet, N.; Fabbri, A.; Gaucher, E.C. Thermoddem: A Geochemical Database Focused on Low Temperature Water/Rock Interactions and Waste Materials. *Appl. Geochem.* **2012**, *27*, 2107–2116. [[CrossRef](#)]
56. Johnson, J.W.; Oelkers, E.H.; Helgeson, H.C. SUPCRT92: A Software Package for Calculating the Standard Molal Thermodynamic Properties of Minerals, Gases, Aqueous Species, and Reactions from 1 to 5000 Bar and 0 to 1000 °C. *Comput. Geosci.* **1992**, *18*, 899–947. [[CrossRef](#)]
57. Gil, A.; Trujillano, R.; Vicente, M.A.; Korili, S.A. Analysis of the Structure of Alumina-Pillard Clays by Nitrogen and Carbon Dioxide Adsorption. *Adsorpt. Sci. Technol.* **2007**, *25*, 217–226. [[CrossRef](#)]
58. Do, D.D. *Adsorption Analysis: Equilibria and Kinetics: (With CD Containing Computer Matlab Programs)*; Series on Chemical Engineering; Imperial College Press: London, UK; World Scientific: Singapore, 1998; Volume 2, ISBN 978-1-86094-130-6.
59. Carcione, J.M.; Gei, D.; Picotti, S.; Misnan, M.S.; Rashidi, M.R.A.; Bakar, Z.A.A.; Harith, Z.Z.T.; Bahri, N.H.S.; Hashim, N. Porosity and Permeability of the Overburden from Wireline Logs: A Case Study from Offshore Malaysia. *Geomech. Geophys. Geo-Energy Geo-Resour* **2020**, *6*, 48. [[CrossRef](#)]
60. Clauser, C.; Huenges, E. Thermal Conductivity of Rocks and Minerals. *Rock Phys. Phase Relat. A Handb. Phys. Constants* **1995**, *3*, 105–126.
61. Clauser, C. The Thermal Regime of the Earth and Heat Transport Processes in the Earth's Crust. *Surv. Geophys.* **2006**, *30*, 163–191. [[CrossRef](#)]
62. Cantucci, B.; Montegrossi, G.; Lucci, F.; Quattrocchi, F. Reconstruction of Rocks Petrophysical Properties as Input Data for Reservoir Modeling: Rocks Petrophysical Properties. *Geochem. Geophys. Geosyst.* **2016**, *17*, 4534–4552. [[CrossRef](#)]
63. Wu, W.; Reece, J.S.; Gensterblum, Y.; Zoback, M.D. Permeability Evolution of Slowly Slipping Faults in Shale Reservoirs. *Geophys. Res. Lett.* **2017**, *44*, 11368–11375. [[CrossRef](#)]
64. Duan, Z.; Sun, R. An Improved Model Calculating CO<sub>2</sub> Solubility in Pure Water and Aqueous NaCl Solutions from 273 to 533 K and from 0 to 2000 Bar. *Chem. Geol.* **2003**, *193*, 257–271. [[CrossRef](#)]
65. Duan, Z.; Sun, R.; Zhu, C.; Chou, I.-M. An Improved Model for the Calculation of CO<sub>2</sub> Solubility in Aqueous Solutions Containing Na<sup>+</sup>, K<sup>+</sup>, Ca<sup>2+</sup>, Mg<sup>2+</sup>, Cl<sup>-</sup>, and SO<sub>4</sub><sup>2-</sup>. *Mar. Chem.* **2006**, *98*, 131–139. [[CrossRef](#)]
66. Heinemann, N.; Haszeldine, R.S.; Shu, Y.; Stewart, R.J.; Scott, V.; Wilkinson, M. CO<sub>2</sub> Sequestration with Limited Sealing Capability: A New Injection and Storage Strategy in the Pearl River Mouth Basin (China). *Int. J. Greenh. Gas Control* **2018**, *68*, 230–235. [[CrossRef](#)]
67. Ukaegbu, C.; Gundogan, O.; Mackay, E.; Pickup, G.; Todd, A.; Gozalpour, F. Simulation of CO<sub>2</sub> Storage in a Heterogeneous Aquifer. *Proc. Inst. Mech. Eng. Part A J. Power Energy* **2009**, *223*, 249–267. [[CrossRef](#)]
68. Weniger, P.; Kalkreuth, W.; Busch, A.; Krooss, B.M. High-Pressure Methane and Carbon Dioxide Sorption on Coal and Shale Samples from the Paraná Basin, Brazil. *Int. J. Coal Geol.* **2010**, *84*, 190–205. [[CrossRef](#)]
69. Siemons, N.; Busch, A. Measurement and Interpretation of Supercritical CO<sub>2</sub> Sorption on Various Coals. *Int. J. Coal Geol.* **2007**, *69*, 229–242. [[CrossRef](#)]
70. Chi, Y.; Zhao, C.; Lv, J.; Zhao, J.; Zhang, Y. Thermodynamics and Kinetics of CO<sub>2</sub>/CH<sub>4</sub> Adsorption on Shale from China: Measurements and Modeling. *Energies* **2019**, *12*, 978. [[CrossRef](#)]
71. Rex, R.W. Clay Mineral Formation in Sea Water by Submarine Weathering of K-Feldspar. *Clays Clay Miner.* **1966**, *14*, 235–240. [[CrossRef](#)]

**Disclaimer/Publisher's Note:** The statements, opinions and data contained in all publications are solely those of the individual author(s) and contributor(s) and not of MDPI and/or the editor(s). MDPI and/or the editor(s) disclaim responsibility for any injury to people or property resulting from any ideas, methods, instructions or products referred to in the content.